PCCP

Ab initio modeling of H_2S dissociative chemisorption on Ag(100)

Journal:	*Physical Chemistry Chemical Physics*
Manuscript ID	CP-ART-12-2021-005612.R1
Article Type:	Paper
Date Submitted by the Author:	11-Jun-2022
Complete List of Authors:	RAMOTHE, Vivien; ISTerre, ; PNNL, Charlet, Laurent; Université Grenoble Alpes, ISTerre Gilbert, Benjamin; Lawrence Berkeley National Laboratory, Earth Sciences Division Sassi, Michel; Pacific Northwest National Laboratory, Physical Sciences Division Simonnin, Pauline; PNNL, Rosso, Kevin; Pacific Northwest National Laboratory, Physical Sciences Division

ARTICLE

Received 00th January 20xx,
Accepted 00th January 20xx

DOI: 10.1039/x0xx00000x

Ab initio modeling of H_2S dissociative chemisorption on Ag(100)

Vivien Ramothe,*[a] Laurent Charlet,[a] Benjamin Gilbert,[b] Pauline Simonnin[c], Michel Sassi,[c] Kevin M. Rosso[c]

Natural sulfidation of silver nanomaterials can passivate the surface, while preserving desirable optical and electrical properties, which is beneficial for limiting Ag^+ release and cytotoxicity. But little is known at the atomic scale about silver sulfidation mechanisms, particularly on different crystallographic terminations. Using density functional theory (DFT) calculations, we examined the process of H_2S sorption and reaction on Ag(100) surfaces relevant to Ag nanowires (AgNWs). DFT energy minimizations predict a strong dissociative chemisorption of H_2S on the surface yielding co-adsorbed sulfide and hydrogen atoms in specific surface sites. However, nudged elastic band (NEB) calculations suggest relatively large activation energies for both the first and second dissociation steps, due in part to overcoming the energy to cleave the S-H bond and attendant site migration from an on-top Ag site position to a hollow site position of the bound S atom. The large barriers associated with the dissociative chemisorption reaction for gas-phase H_2S points to the importance of including thermochemical contributions and the influence of other components in more complex environmental media such as air or water to help complete the mechanistic picture of silver sulfidation and passivation for realistic systems.

INTRODUCTION

Understanding the sulfidation of silver-based nanostructures is important both for supporting their increasing deployment in modern industry and developing risk-mitigation strategies for their fate in the environment. Silver metal naturally reacts with sources of sulfur in air at ambient conditions, which can create an Ag_2S-like passivation layer.(1,2) The resulting silver sulfide possesses temperature-dependent conductivity ranging from semiconducting to superionic due in the latter case to highly mobile silver ions in the sulfur sub-lattice.(3) Thin films of silver sulfide have applications in photoconducting and photochemical cells(4,5), in sensors(6), infrared detectors(7) and as solar selective coatings for conversion of solar energy into electricity (8,9). Quantum dots of sulfides, including Ag_2S, are being intensively studied for fluorescent labels in biology and medicine(10–15). And the well-known antibacterial properties of silver nanostructures has led to their development as anticancer agents,(16,17) and antimicrobial agents for medical applications(18–22) or wastewater treatment.(23) But it remains unclear how sulfidation influences reaction outcomes.

The case of silver nanowires (AgNWs) is of particular interest because it is under review for cytotoxicity risks to different organisms that these nanomaterials might ultimately be in direct contact with(20,24,25). Typically a few nanometers wide by up to several tens of micrometers long, AgNWs combine high conductivity with low optical extinction leading to promising device applications. The main issue is the possibility of Ag^+ release and the higher potential for cellular entry induced by the wire shape. Sulfidation may limit Ag^+ release and cytotoxicity by preventing AgNW dissolution(19,21,26) while apparently maintaining their desirable optical properties.(8,27–30) But because the atomic structure of tip and side surface terminations of AgNWs are different, developing a fundamental understanding of surface-specific sulfidation mechanisms could help improve strategies for AgNW design by selecting surfaces with beneficial passivation behavior. In general, sulfidation of silver nanomaterials is of great interest for limiting degradation and increasing life expectancy of newly designed devices.

[a] Univ. Grenoble Alpes, Univ. Savoie Mont Blanc, CNRS, IRD, IFSTTAR, ISTerre, Grenoble, France.
[b] Earth Science Division, Lawrence Berkeley National Laboratory, Berkeley, California 94720
[c] Physical Sciences Division, Physical and Computational Sciences Directorate, Pacific Northwest National Laboratory, Richland, Washington 99352, United States

H_2S is the simplest source of sulfide that can directly react with Ag to form Ag_2S. Although many studies have been devoted to understanding the sulfidation of various sorbents,(25,31–34) little is known about H_2S adsorption and reaction pathways on Ag. The sulfidation reaction $2Ag^0 + S^{2-} \rightarrow Ag_2S$ requires an oxidant to be correctly balanced. In anaerobic environments where H_2S concentrations are significant, gaseous or dissolved O_2 is in limited supply. The redox interactions that enable sulfidation in natural environments are thus complex. Here we elect to study the process of H_2S adsorption and reaction on Ag surfaces a first step in unravelling AgNW sulfidation.

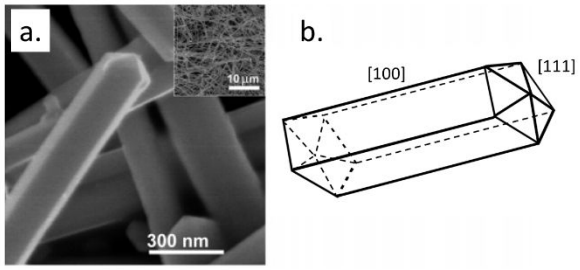

Figure 1a.) Scanning electron micrograph of typical AgNWs, b.) schematic view of relevant crystallographic terminations. a. Reprinted with permission from Elechiguerra, J. L.; Larios-Lopez, L.; Liu, C.; Garcia-Gutierrez, D.; Camacho-Bragado, A.; Yacaman, M. J. C

Silver nanowires typically have a pentagon shaped cross-section with the crystal plane (100) expressed on the sides of the wire and the (111) planes expressed on the tips (Fig. 1a,b.). (35) Because the (100) termination dominates the total surface area, we choose to focus our study on this specific surface. The goal was to examine the reaction barrier for each elementary step leading to the dissociative chemisorption of H_2S on Ag(100), which in the complete atomization limit is represented by:

$$H_2S \xrightarrow{atomization} S + 2H$$

To provide basic insight into the dissociation mechanism, we considered the surface reaction in vacuo. We used density functional theory (DFT) combined with nudged elastic band (NEB) calculations to access relevant surface and molecular properties, structural parameters, activation and reaction energies(31,36–40). Important contributions about the adsorption and dissociation mechanism of H_2S on metal and metal oxide catalysts have been made previously using *ab initio* methods (32,38,41–44). In most cases, the following reactions are of primary interest:

$$H_2S\ (ads) \rightarrow SH\ (ads) + H\ (ads) \quad (1)$$

$$SH\ (ads) \rightarrow H\ (ads) + S\ (ads) \quad (2)$$

Indeed, the dissociation pathway studied here involves sequential abstraction of H atoms from H_2S adsorbed on Ag(100). We investigated the reaction barrier for each elementary step of H–S bond cleavage yielding Ag–S and Ag–H hydride surface groups. By providing a better understanding of these first steps of Ag(100) sulfidation by H_2S, future work can compare the same process on other terminations and ultimately be extended to examine multilayer formation and passivation.

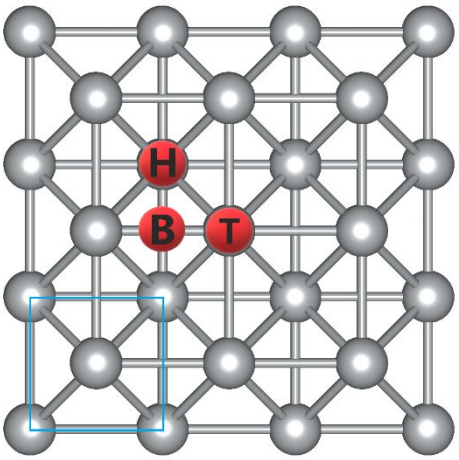

Figure 2 Top view of the adsorption sites on Ag(100) 3 × 3 supercell: on-top site (T), two-fold bridge site (B), four-fold hollow site (H). Unit cell is shown in black solid lines in bottom left corner.

COMPUTATIONAL METHODS

All calculations were carried out with periodic boundary conditions (PBC) in the plane-wave Vienna Ab initio Software Package (VASP) (45,46) electronic structure code. The simulations were performed within the gradient generalized approximation (GGA) with the exchange−correlation functional of Perdew, Burke and Ernzerhof (PBE) (47). The plane-wave calculations were carried out under the projector-augmented wave method with a kinetic energy cutoff of 400 eV (48). The total energy convergence criteria were set to be within 10^{-5} eV with a Gaussian smearing width of 0.05 eV to improve the convergence of orbital energies. The vacuum region between the two silver surfaces has been set to 30 Å (unless stated otherwise) to eliminate spurious interactions between the adsorbate and the periodic image of the bottom layer of the surface.

The Ag(100) surface, as shown on Figure 2, has three high symmetry adsorption sites: one at the top of an Ag at the surface (top site, T), one between two of them (bridge site, B) and one between four of them (hollow site, H). Our study considered all three sites as potentially active reaction sites.

We calculated the adsorption energy of the adsorbate species, ΔE, using the expression:

$$\Delta E = \frac{E_{Ag\ slab} + E_{adsorbate} - E_{total}}{2} \quad (3)$$

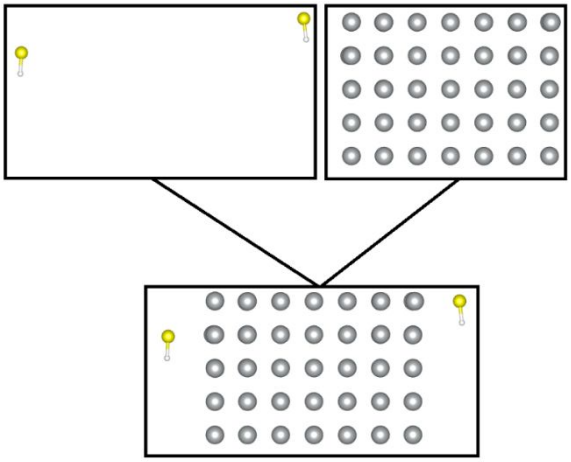

Figure 3. Schematic view illustrating the modeling approach. In order to get adsorption energy (Eq.3), electronic density deformation (Eq.4) and charge transfer analysis, we separated the substrate from the adsorbate and ran calculations on each individually.

where E_{total} is the total energy of the silver slab with the H_2S adsorbed on the surface, $E_{Ag\ slab}$ is the total energy of the slab, and $E_{adsorbate}$ is the total energy of adsorbate in gas phase (H_2S, SH/H or S/H/H). We must divide by two the result because we have a molecule symmetrically adsorbed on each side of the slab. Based on this definition, the larger the ΔE is, the more thermodynamically favorable is the adsorption. The procedure used to separately calculate the adsorbate and silver energy from the total system is schematically represented in Figure 3. To investigate changes in the electronic structure when the solute is adsorbed on the surface, we calculated the deformation charge density, Δρ(**r**), which includes a direct comparison to the non-sorbed state:

$$\Delta\rho(\mathbf{r}) = \rho_{total}(\mathbf{r}) - (\rho_{Ag\ slab}(\mathbf{r}) + \rho_{adsorbate}(\mathbf{r})) \quad (4)$$

where $\rho_{total}(\mathbf{r})$, $\rho_{Ag\ slab}(\mathbf{r})$ and $\rho_{adsorbate}(\mathbf{r})$ are electron densities of the total system, the silver slab and the adsorbate in gas phase, respectively.

We studied the charge transfer by comparing the Bader charges(49–52) between the slab surface and the gas phase molecule with the adsorbed state. We evaluated the strength of bonds between the adsorbates and the surface by calculating the charge density at (3,–1) bond critical points $\nabla\rho(\boldsymbol{r})_{cp}$, corresponding to the zero-values of the gradient: $\nabla\rho(\boldsymbol{r}) = 0$. These saddle points correspond to a minimum in the charge density along a bond path, providing a measure of the strength of bonding in terms of the electronic overlap.

RESULTS AND DISCUSSION

H_2S adsorption on Ag(100).

We first investigated the adsorption of H_2S. Here, 12 initial configurations were relaxed with the molecule oriented with either the two H-S bonds parallel to the surface (Fig. 4a, b), or one parallel and the other one pointing away from the surface (Fig. 4c,dc, d) We distinguish them as parallel versus perpendicular orientations. Figure 4 is an example of four initial configurations tested on the H-site of the silver surface. In this work the optimized silver matrix is face centered cubic with a lattice parameter of 4.08 Å in the bulk, that extends to 4.15 Å at the surface.

Energy minimization of all 12 configurations led to one optimal configuration with H_2S parallel to the surface. We found that the adsorption site with the largest adsorption energy is the T-site (Fig. 2), such that even when starting a calculation with H_2S facing the H site, the molecule easily migrates to face the T-site. Two different configurations, with either H pointing toward H- or B-sites, have a remarkably similar adsorption energy, with a slight preference for the orientation toward the B site (0.184 eV vs 0.182 eV) (Fig. 5). All other configurations of hydrogen sulfide adsorbed on the silver surface that converged have an adsorption energy ranging between 0.056 eV and 0.169 eV.

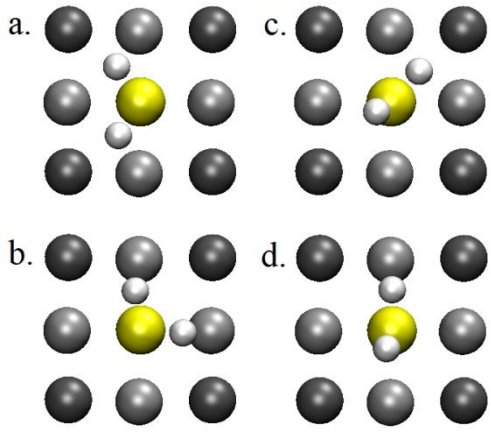

Figure 4 Examples of initial configurations tested on the hollow site (H). Panels a.) and b.) have H2S parallel to the silver surface with H-S bonds respectively pointing toward the bridging site (B) and the top site (T), while c.) and d.) have one H-S bond point

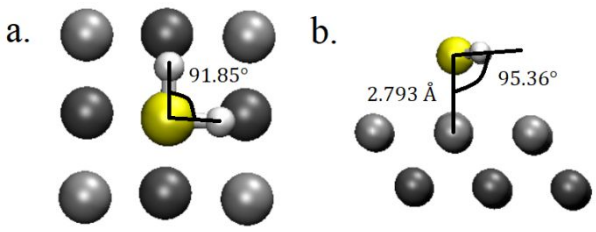

Figure 5 Largest adsorption energy configuration of H2S on Ag(100) with a.) the top view of the configuration and b.) the side view.

All the bond lengths and the binding charge densities calculated for the systems studied are summarized in Table 1.

	$\Delta\rho(\boldsymbol{r})_{cp}$ (e⁻/Å³)		Bond length (Å)		Adsorption energy (eV)
	S-Ag	H-Ag	S-Ag	H-Ag	
H_2S	0.02	-	2.79	-	0.184
HS/H	0.10	0.55	2.21	2.79	4.50
S/H/H	0.07	0.10	2.52	2.11	8.21

Table 1 Binding charge density, bond length values and adsorption energies for the most energetically favorable configurations of the three states of H2S decomposition on the surface.

In the highest energy structure, the H—S and S—Ag bond lengths are 1.352 and 2.793 Å respectively, while the H-S-H angle is 91.85° (angle is computed to be 91.57° for the free gas phase H_2S molecule). In fact, the H_2S molecule is not exactly parallel to the surface; the sulfide atom is slightly pointing toward the T-site silver atom with an Ag-S-H angle of 95.36°. The H—S bond length for the H_2S molecule in its adsorbed state is slightly longer (0.2%) than in the gas phase (1.349 Å), and the H-S-H angle is slightly wider. This indicates that the strength of the H—S bond becomes weaker due to the adsorption, consistent with promotion of dissociation. We also found that the binding charge density at the critical point for the S—Ag bond is 0.019 e⁻/Å³ (see Table 1) which may be qualitatively equated to a weak O—H bond (53).

In Figure 6, we present the deformation of the electronic structure of this configuration, obtained through the procedure explained in the Methods section and in Figure 3. We show the electron density difference between the gas phase hydrogen sulfide and silver slab, with in blue depletion and in red accumulation of electron density. It shows here that the electron density of both H_2S and silver is depleted, while there is an accumulation of electrons between the sulfide and the surface. Indeed, electrons move in this latter region to create a bond between S and the surface silver atom. As expected, this mixing of the electron density points toward chemisorption. The charge density analysis revealed that the electron density shared between H_2S and its facing Ag atom is equivalent to the density shared between two bulk Ag atoms. This evidence further supports the notion that the H_2S molecule has a strong interaction with the Ag surface. According to the Bader charge analysis (49–52), the S atom lost 1.5 e⁻ between H_2S in gas state and in adsorbed state, while there is no significant loss of charge for the H atom nor for the Ag atom interacting with H_2S. This charge is delocalized from the S atom to the red area between S atom and silver surface to form a bond, equivalent in strength to an H-bond.

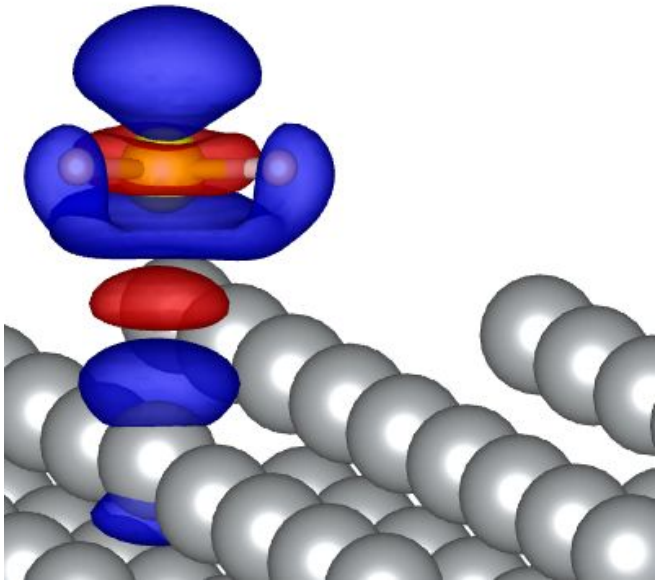

Figure 6. Deformation of the electronic density of H2S adsorbed on [100] silver surface compared to H2S in gas phase. The blue and red isosurface values (10^{-3} e⁻/Å²) respectively represent a depletion and accumulation of electrons.

This red area is also the location of the S-Ag bond's critical point. The silver atom interaction with the adsorbate does not exhibit any loss of charge. This could be explained by the

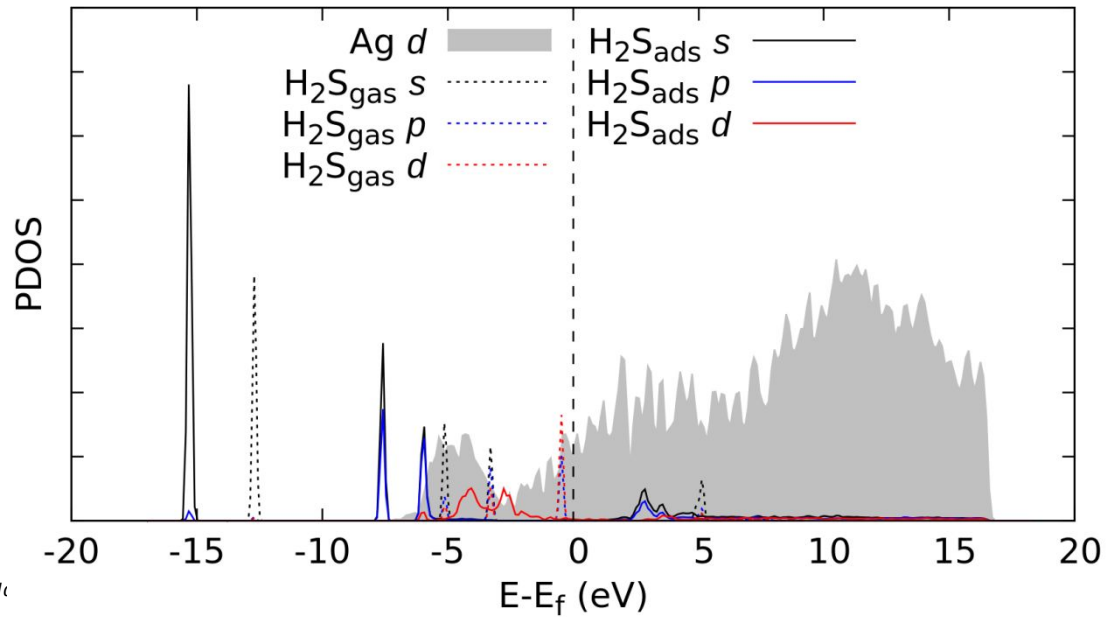

Figure 7 Projected density of states comparison between the d orbital of the silver (grey area) and the s, p and d orbitals of H2S in gas phase (dashed lines) and in adsorbed state (solid lines).

conducting nature of the silver slab that largely compensates loss of charges on this fine scale.

Figure 7 shows the projected density of state (PDOS) of the silver *d* orbitals in filled grey area, compared to the *s*, *p* and *d* molecular orbitals of H_2S respectively in dashed black, blue and red lines for the gas state, and solid lines for the adsorbed state. The Fermi level energy (E_f) is set as the reference in all cases. For adsorbed H_2S molecule, the low energy *s* orbitals are positioned at -15.31 eV followed by two sharp peaks at -7.57 eV and -5.93 eV with *sp* hybridization. H_2S molecular *d* orbitals are spanning an energy range from -4.75 eV to -1.82 eV. The first peak of the *d* orbitals of the silver slab is located at -5.70 eV, which is similar to the energy of peak of $H_2S_{(ads)}$ on the *p* orbital at -5.93 eV, suggesting a possible binding interaction. We observe a clear shift in lower energies for the first three peaks going from gas to adsorbed phase. The *s* orbitals peaks localized at -12.71 eV, -5.13 eV, and -3.29 eV for $H_2S_{(g)}$ respectively shift in energy to -15.31 eV, -7.58 eV, and -5.93 eV for the adsorbed H_2S. The fourth peak observed for the gas phase, located at -0.46 eV, belongs to both *p* and *d* orbitals. The shift (around 2.6 eV) and splitting of this last peak is a strong indicator of chemical bonding between H_2S and silver.

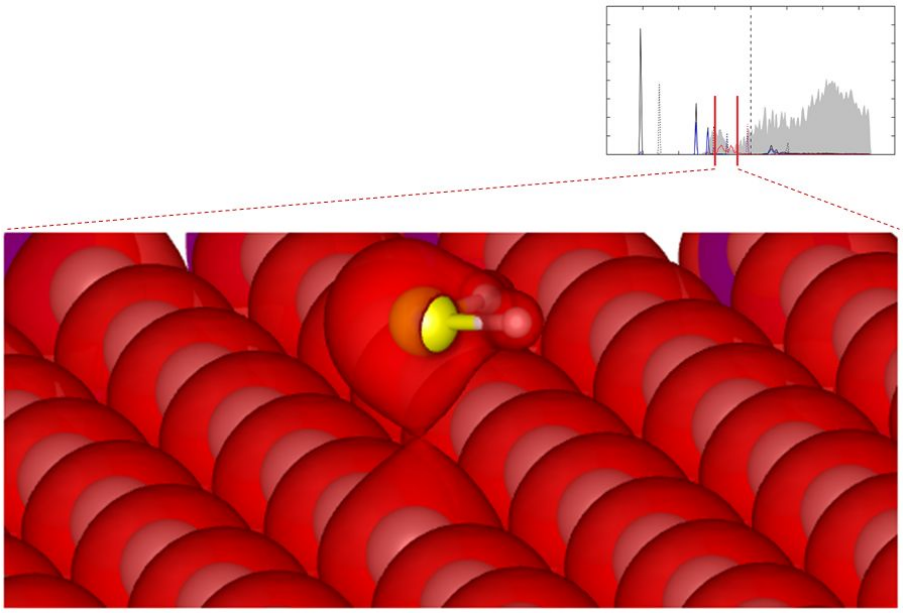

Figure 8 Local density of states (LDOS) integrated between -5.0 eV and -2.0 eV for the H2S adsorption on Ag(100) surface. The isosurface is at 3.1×10^{-2} $e^{-}.Å^{-3}$.

Figure 8 is the volumetric representation of the electron density integrated in an energy range relevant to the *d* orbitals (i.e., between -5.0 eV and -2.0 eV) of H_2S, mixed with those of the silver surface. The isosurface is at 3.1×10^{-2} $e^{-}.Å^{-3}$, at this level we can see that these electrons belong to both the H_2S absorbed molecule and the silver atom interacting with it. This result is another proof of the formation of a chemical bond between the silver surface and the H_2S molecule.

To summarize the results for the first step of H_2S adsorption on the Ag(100) surface, we find compelling evidence for strong chemisorption preferentially on the T-site. It is worth mentioning that the adsorption energies are calculated from the relaxed configurations in both states (adsorbed and desorbed) in order to account for interaction energies and system deformation. This approach is consistent with the main conclusions from Zhang et. al., that state the importance of dimensionality of chemisorption at metallic interfaces.(54) Moreover, the magnitude of the calculated adsorption energies is consistent with similar reactions studied previously such as, for example, water on Ni(111).(55–58) The charge density in the area between the S and the closest Ag is of the same order of magnitude than between two silver atoms in the bulk. The adsorption energy proves that this interaction is strong enough to make this configuration thermodynamically favorable. Adsorption leads to elongation of H-S bonds, which could in turn promote the dissociation, which we examine in a subsequent section.

HS and H co-adsorption on Ag(100).

We next examined configurations for co-adsorbed HS and H fragments to assess stable dissociated configurations and dissociation energies. We examined 27 possible configurations of co-adsorbed HS and H fragments. For clarity, the H atom that remains bonded to the S will be referred to as H_a, the bound SH molecule will be referred to as H_aS, and the dissociated H will be referred to as H_b. We characterize these configurations first based on the posture of the H_aS fragment: parallel with the H_a pointing to the B-, H- or T-sites, or perpendicular to the surface. In addition, there are three possible adsorption sites to investigate for the atomized H_b atom. We identified the most stable of these configurations to have the H_aS fragment perpendicular to the surface on top of the B-site with S facing the surface. The remaining H_b atom is above an adjacent B-site, as depicted in Figure 5. In this

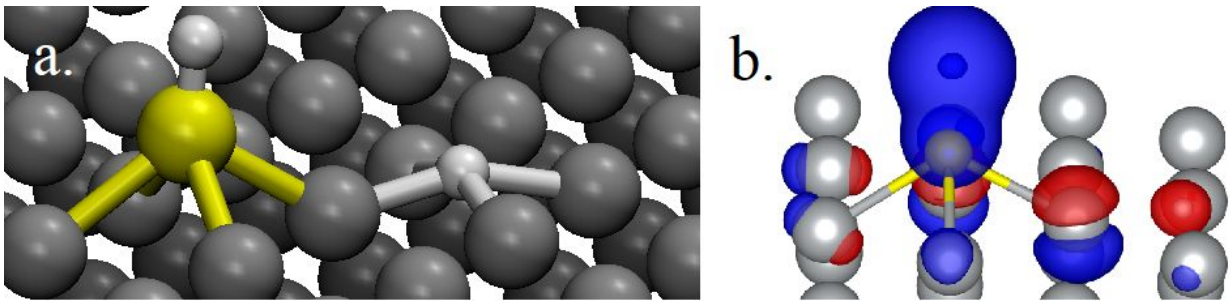

Figure 9 a.) Configuration corresponding to the largest co-adsorption energy of HaS/Hb on Ag [100] surface, and b.) the deformation of the electron density associated to this configuration with the increase of electron density is in red and the decrease in blue.

configuration, the S-Ag distance is 2.21 Å, which is 26.2% shorter than in the H_2S adsorption case (2.79 Å). The S-H_a bond length is also slightly smaller (0.7%) than in the adsorbed H_2S case with 1.34 Å (vs 1.35 Å). The atomized H_b forms a square based pyramid with four Ag atoms from the surface, standing 2.79 Å away. This highlights that after atomization, the interaction of the two adsorbates with the surface is stronger than in the H_2S case.

This is clearly reinforced by energetic considerations. Indeed, the dissociation of H_2S into H_aS and H_b at the surface is energetically favorable, as expected from previous work (41,42). The atomized configuration has an adsorption energy of 4.50 eV whereas for the H_2S chemisorbed on the Ag [100] surface the energy is only 0.18 eV. The binding charge densities of both S-Ag bond and H_b-Ag bond were found to be respectively 0.09 $e^-/Å^3$ and 0.55 $e^-/Å^3$. The charge density of the S-Ag bond is much higher (by a factor 3.73) than in the H_2S adsorption case, which is consistent with the contraction of the S-Ag bond length. The charge density of the H_b-Ag bond is, as expected, much higher, qualitatively consistent with a strong O-H (around 0.3 $e^-/Å^3$) interaction (53).

The most stable configuration is displayed in Figure 9a and the corresponding deformation of the electron density in Figure 9b. It shows a charge density decrease on the H_aS molecule compared to the gas phase and an increase between the molecule and the silver surface, which means that the H_aS molecule loses some electron density to form a bond with the silver surface. Because the silver surface is a conductor, there is no significant charge density decrease on the silver atoms interacting with the H_aS molecule. As expected, there is an increase of charge density on the remaining H_b atom interacting with the surface. According to a Bader charge analysis of the adsorbed H_aS fragment, the S atom gained 0.55 e^- compared to the same molecule in gas phase, while the H atom gained 0.13 e^-, which means the total charge transfer between H_aS and the silver surface is 0.68 e^-. Finally, the

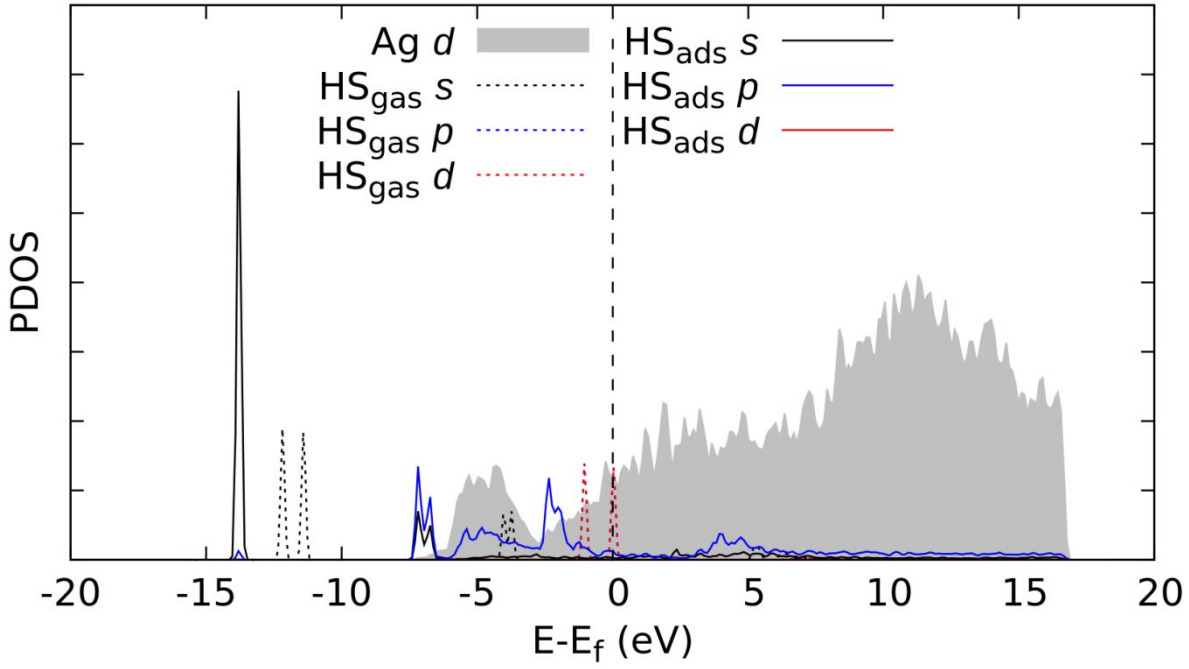

Figure 10 PDOS comparison between the d orbitals of silver (grey area) and the s (black), p (blue) and d (red) orbitals of the HS molecule in gas phase (dashed line) and in adsorbed state (solid lines).

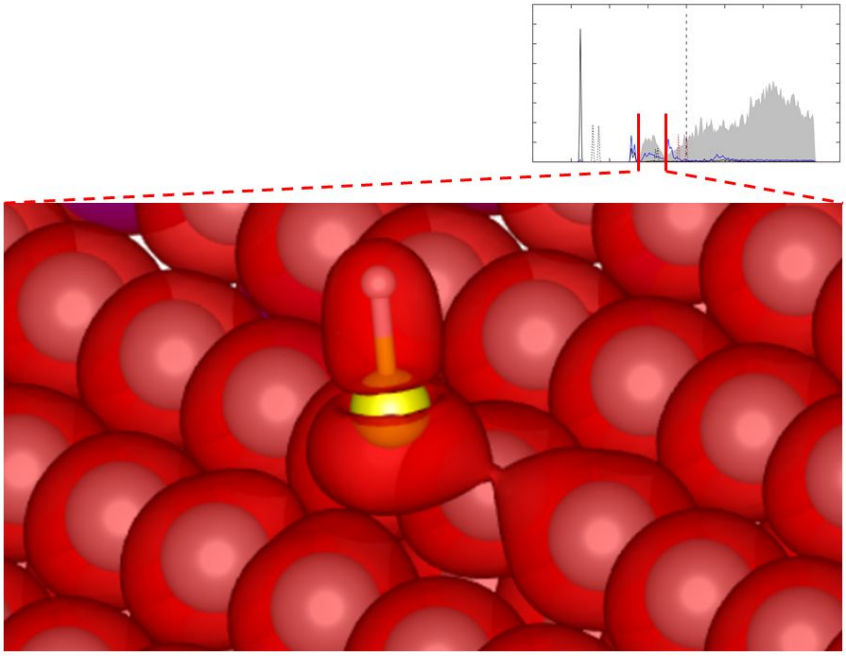

Figure 11 Local electronic density of states (LDOS) integrated between -7.10 eV and -3.50 eV for the HaS adsorption of silver surface. The isosurface is at 2.91×10-2 e-.Å-3

atomized H atom on the surface gained 0.2 e^-. Compared to the H_2S molecule in adsorbed state the S atoms see an increase of 1.64 e^- and 0.1 e^- for the H_b atom of the H_aS molecule. The charge density observations are consistent with the shortening of the bond length compared to the H_2S adsorption case and the increase of the adsorption energy.

Using the PDOS we can compare the H_2S adsorption, and the first atomized state (H_aS/H_b) adsorbed on the silver surface. Figure 10 shows the PDOS of the *d* orbitals of silver compared to the *s*, *p* and *d* orbitals of the HS molecule in gas phase (dashed lines) and in adsorbed state (solid lines). The Ag *d* orbitals display wide peaks of available states below the fermi level extending from -7.19 eV to -2.71 eV that correspond to H_aS *p* orbitals available states. Concurrently, for H_aS molecule the deeper level of valence band is positioned at -13.80 eV and belongs to the *s* orbitals and is followed by two peaks of populated states going from -7.29 eV to -6.50 eV with *sp* hybridization, and then a wide range of populated states in the *p* orbitals extending from -5.60 eV to -3.02 eV and a last peak centered at -2.35 eV. The two peaks centered at -1.04 eV and 0.4 eV are *pd* hybridized and do not remain in the adsorbed state. These populated states shift to the lower energies and become purely *p* or *sp* hybridized. Since one of the peaks fits to the populated states of the silver *d* orbitals, we focused the visualization of the partial charge in the energy range between -7.10 eV and -3.50 eV.

As we did for the H_2S adsorption case, we integrated the electronic density of states from -7.10 eV to -3.50 eV (see Figure 11). The H_aS molecule in this configuration shares electrons between one of the four closest silver atoms that can be found around the B site. The isosurface is at 2.91×10^{-2} $e^-.Å^{-3}$, which is the highest value of the charge density at critical point of the first S-Ag bond. The lowest value of isosurface allowing continuity between silver and adsorbate is 2.65×10^{-2} $e^-.Å^{-3}$, which makes a range of charge density of 4.8×10^{-3} $e^-.Å^{-3}$ between the first end the fourth S-Ag bond. This narrow range is relevant with the dispersion of the Ag-S bond length: 3.30×10^{-2} Å.

The H_aS/H_b co-adsorption is thus thermodynamically more favorable compared to the H_2S chemisorption alone. There is an evident correlation between the deformation of the charge density, the density of charge at the critical point and the contraction of the Ag-S bond compared to H_2S adsorbed. Yet, the charge density at the critical point indicates that the Ag-S bond appears to be comparable to a weak hydrogen bond, which is consistent with the electronic density in the energy range where silver and H_aS orbitals overlap and is a proof of the formation of a chemical bond between the HS adsorbate and the silver surface.

Given our observations for the H_aS/H_b chemisorption on the silver surface, this likely defines the product state for the first dissociation step, which would entail S first located over the T-site when in the form of H_2S, followed by S located in the B-site after dissociation. Before considering the activation energy for this first dissociation step, we first examine the possibility that the second dissociation step leading to S/H/H co-adsorption is also energetically favorable.

S and two H co-adsorption on Ag(100).

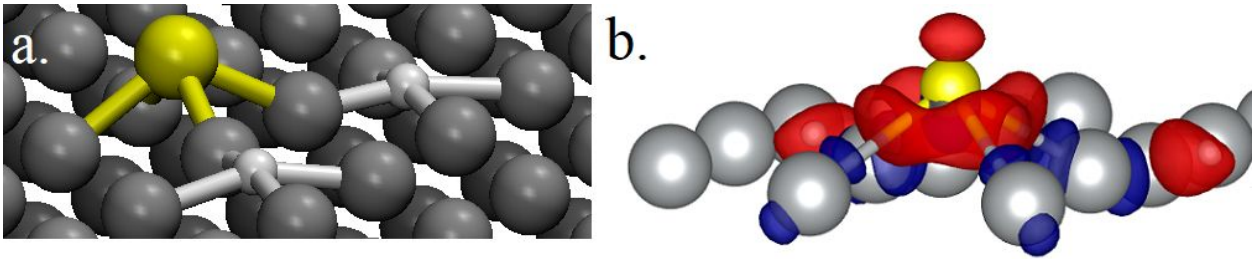

Figure 12 a.) View of the most stable configuration of co-adsorption of S/Ha/Hb on [100] silver surface, and b.) the deformation of electron density of the most stable S/Ha/Hb adsorption configuration on Ag [100] with the increase of electron density (5×10-3 e-.Å

In the $S/H_a/H_b$ co-adsorption case, we counted 27 initial configurations determined by the positions of the three adsorbates (two H and one S) on the three possible adsorption sites. Figure 12 shows the configuration found to be the most favorable in energy. Adsorbing the two H_a and H_b atoms on two H-sites next to each other seems to be a more straightforward path, but the repulsive interaction between the two H atoms is too strong to converge while maintaining the configuration as it is. Actually, in the most stable configuration, the two H atoms need to be separated by at least one unit cell (Fig. 12a). This configuration has an adsorption energy of 8.21 eV, which is larger than both the H_aS/H_b (4.35 eV) and the H_2S (0.18 eV). Ignoring for the moment specific reaction pathways and energy barriers separating adsorption configurations, adsorption energy considerations taken alone indicate that dissociative chemisorption of H_2S on Ag(100) should proceed to complete two-step atomization on the surface.

In this configuration, the length of the S-Ag bond is 2.52 Å, so slightly larger than the one in H_aS/H_b co-adsorption case, suggesting that S atom in the H_aS/H_b co-adsorption system has the strongest interaction with Ag. In fact, the S atom in this configuration is free to form 4 bonds with the 4 surrounding silver atoms which makes the overall configuration more stable than the H_aS adsorption case, despite the S-Ag bond stretching. In addition, the two H atoms tend to bind at the H-sites just adjacent to the S atom. The Ag-H bond length is 2.11 Å, shorter than the 2.79 Å from the H_aS adsorption case, suggesting a stronger interaction.

As in the previous case with H_aS/H_b co-adsorption, the S atom here is interacting with four neighboring Ag atoms, which increases the area where the electron density is deformed (Fig. 12b). We calculated a charge increase of 0.67 e^- on the adsorbed S compared to the gas phase, confirming that despite the increase of the S-Ag bond length, the interaction between the S atom and the silver surface is stronger than in the H_2S and H_aS cases. The two H_a and H_b atoms interacting with the silver surface have the same Bader charges than the H_b in the H_aS/H_b case. The S atom charge increases here, compared to the previous atomization step, which is also a consequence of the S-H_a interaction drawing electronic density

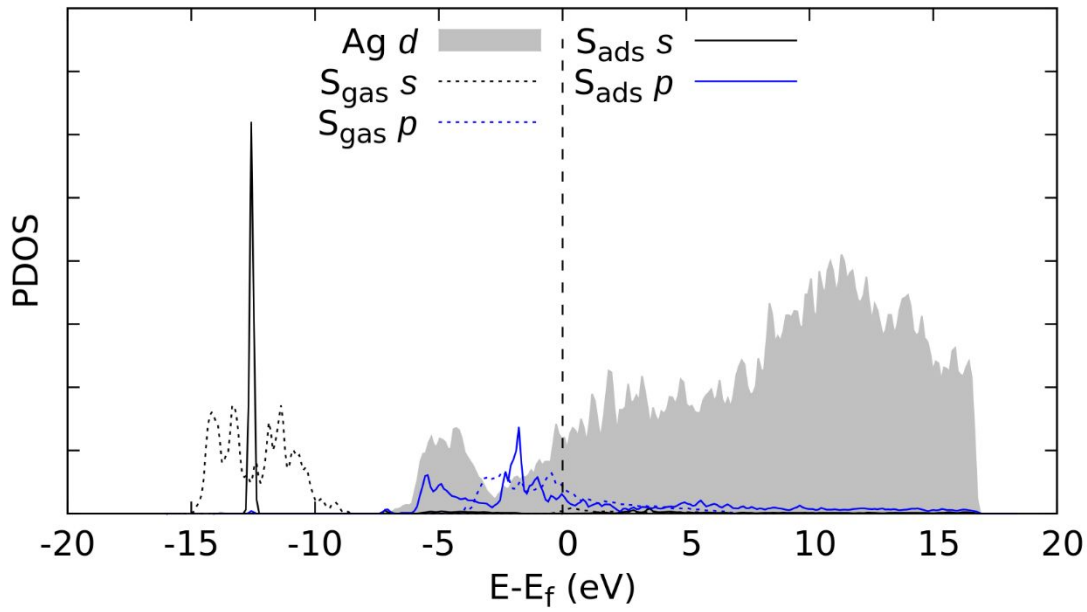

Figure 13 PDOS comparison between the d orbital of silver (grey area) with the s (black) and p (blue) orbitals of the S atom in gas phase (dash) and in adsorbed state (line).

out of the S atom to maintain the H_aS bond. The red bulb on the S atom in Figure 12b illustrates that phenomenon.

We compared the PDOS for the adsorbed S atom with that in gas phase in Figure 13. The silver density of states is close the one we obtained for the two previous steps of the dissociation mechanism, with a wide range of *d* orbital populated states going from -7.19 eV to -2.71 eV. For $S_{(g)}$, we obtained two wide ranges of states extending from -15.06 to -8.82 eV for the *s* orbital and from -4.05 to unpopulated states higher than the Fermi level in the *p*. On one hand, the adsorption of sulfur causes a shift in the lower energies compared to the gas phase for *p* orbitals, that simultaneously divides into two peaks. The splitting and shifting are consistent with the adsorption energy found for this configuration. On the other hand, the *s* orbital peak stays centered around the same energy at -12.57 eV but becomes sharper. The peak of the *p* orbital of $S_{(ads)}$ matches the first *d* orbital peak of Ag between -5.76 eV and -2.83 eV, so we focused on this energy range to visualize the spatial distribution of the charge density.

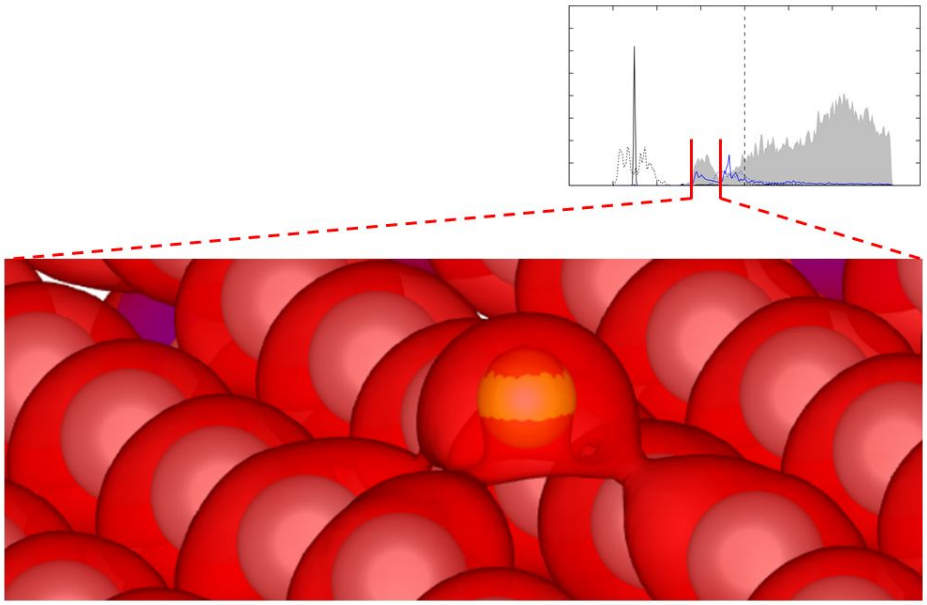

Figure 14 Local electronic density of states (LDOS) integrated between -5.76 eV and -2.83 eV with the isosurface at 5×10-2e-.Å-3 for the S atom adsorbed on the silver surface.

Figure 14 illustrates the electron density for the electrons comprised in the energy range between -5.76 eV and -2.83 eV. At this stage of dissociation, we expect to observe another chemical binding between the S atom and the silver surface. We noticed a continuity of the isosurface at $1.56.10^{-2}$ $e^-.Å^{-3}$. The isosurface value for the first S-Ag bond is 1.56×10^{-2} $e^-.Å^{-3}$ and 1.60×10^{-2} $e^-.Å^{-3}$ for the fourth, which is a range even narrower than in the HS adsorption case. Still, the width of this range is relevant to the range of the Ag-S bond length dispersion (2.17×10^{-3} Å). As explained in detail below, despite it being lower than H_aS-Ag bond, it is in the range of a strong O-H hydrogen bond. (53)

The charge densities of S-Ag and H-Ag are 0.07 $e^-.Å^{-3}$ and 0.10 $e^-.Å^{-3}$ respectively. This is consistent with the bond length variation calculated from H_2S and HS/H adsorption steps. The S-Ag binding charge density is also consistent with the increase of the bond length. However, for the H-Ag, the decrease of the binding charge density and the increase of the bond length seems to be in contradiction, especially because the Bader charge of the H atom remains the same as in H_aS/H co-adsorption case. This seeming discrepancy can be explained by the lack of sufficient excess electron density in the simulation box, given that H atoms at silver surface act as electronic traps. Indeed, H atoms are significantly more electronegative than the other present species, so they tend to attract any available electron density, to the detriment of S in our case.

Activation energies for dissociation steps.

In addition to the discussed energetics and electronic interactions associated with the two dissociative chemisorption steps of H_2S on Ag(100), we also explored the energy barriers along the reaction pathway using the NEB method with the VTST package.(59–63) The results of the NEB calculations for the two-step mechanism are shown in the energy diagram in Figure 15. As one can see, relative to the intervening barrier heights, the minimum energy adsorption configurations *a*, *c* and *e* have quite similar energies. Dissociated configurations *b* and *c* are defined by relatively large activation energies of 0.90 eV and 1.06 eV respectively. The first dissociation step shown in configuration *c* is exothermic by ΔH = -0.08 eV compared to *a,* while the next dissociation step is endothermic by ΔH = +0.02 eV compared to *c*. The NEB results thus indicate that the last dissociation step (from H_aS/H_b to $S/H_a/H_b$) is slightly thermodynamically unfavorable. This apparent contradiction with the calculated adsorption energies presented earlier arises because the adsorption energies were calculated relative to gas-phase $S/H_a/H_b$ species and a clean Ag surface, whereas the ΔH values between the minima in the NEB landscape are all relative to adsorbed configurations. Thus, the NEB landscape assumes a reaction path occurring entirely on the surface and cannot be directly compared to the adsorption energies to deposit configurations a, c, and e directly from the gas-phase.

The large barrier heights likely relate to the substantial changes in S binding sites predicted by our calculations. For example, dissociation of chemisorbed H_2S on the T-site proceeds to SH binding on an H-site, the reaction pathway of which involves migration of S by 2.31 Å and introduction of strain into the original Ag-S bond by elongation by 2.56 Å to ultimately bind in the H-site. The energy associated with cleaving the S-H bond is also relatively large (4.67 eV in gas) with little assistance provided by the strength of any long-range H…Ag surface site interaction. The same explanation can be referred to for the heights of the energy barrier of the second dissociation path (from *c* to *e).*

Notwithstanding, given the apparent dominance of the activation energies on the reaction pathway relative to the energy differences between energy minima, it is clear that kinetics will largely control system behavior, at least in vacuo, and chemisorbed H_2S may not readily dissociate in the absence of elevated temperature or collective effects arising from interactions with other adsorbed H_2S molecules and/or other environmental constituents that would be present in more realistic complex media (e.g., in air or water). In this latter sense, it is noteworthy that interaction with the environment could abstract H atoms from Ag-H hydride surface groups and lower the probability of any backward reaction (from *e* to *c*). This, in turn, would effectively decrease the energy barrier. Other possible influences not encompassed by our calculations that introduce uncertainty in the rate of achieving the final fully dissociated end state include the prospect for diffusion of adsorbed H atoms across the surface away from the S adsorption site or into the Ag bulk matrix as often observed for metal alloys, for example.

Conclusions

In the present work, H_2S, HS/H and H/H/S adsorption systems were investigated through the calculation of stable

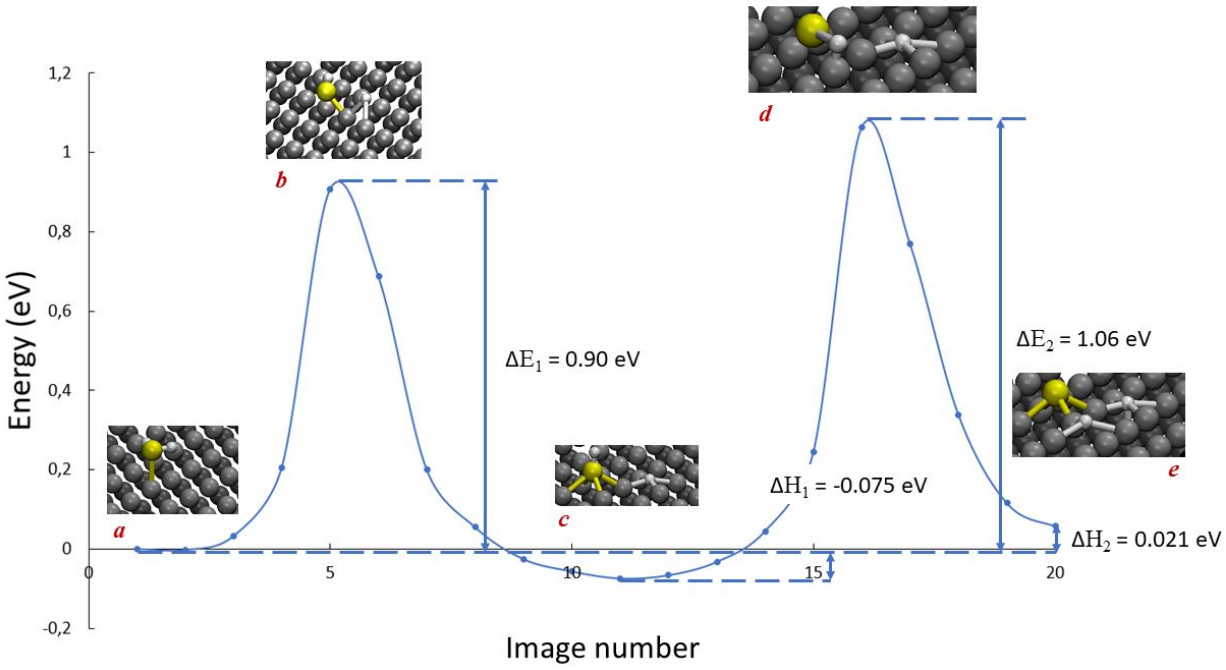

Figure 15NEB results for the two dissociation steps that atomize adsorbed H2S to co-adsorbed S/H/H on Ag(100).

configuration geometries, electron distributions, deformation of these configurations and their electronic density of states using ab initio methods. We were able to highlight favorable two-step dissociation of chemisorbed H_2S on the Ag(100) surface. The most favorable adsorption site of the H_2S molecule is found to be on top of a surface silver atom (i.e., T-site). Following the first dissociation step, the SH adsorbate will migrate from a T-site to an H-site, where S remains after the second dissociation step. During the dissociation process, we found that fragments are chemisorbed at each step via an accumulation of electron density between the sulfide and Ag atom(s) to which it is bonded.

The reaction mechanism we propose is predicted to be thermodynamically favorable although the computed activation energies for the two dissociation steps are relatively large. Because our study only involves minimization of the total electronic energy, future work should attempt to encompass other influences on system behavior such as finite temperature thermochemical contributions. Furthermore, ultimately it is important to consider the probabilities for adsorbed H atoms to diffuse and desorb by interacting with the environment or enter into the bulk Ag metal matrix. In complex environmental media, several different mechanisms could be responsible for desorption the H atoms, which would in turn decrease its surface concentration, thus inhibiting the backward reaction. Although these more complex influences on system behavior are not encompassed in this study, the work helps lay a foundation for more realistic pathways that lead to AgNW sulfidation. It is also crucial to investigate the behavior on other stable terminations of Ag comprising AgNW morphology, such as the (111) tip surfaces.

Conflicts of interest

There are no conflicts to declare.

Acknowledgements

This research was supported by a SERENADE project award for the postdoctoral fellowship of V.R. at the University of Grenoble Alpes under the supervision of L.C., B.G., and K.M.R. (The SERENADE LabEx project received funding from Excellence Initiative of Aix-Marseille University, a French “Investissements d’Avenir” program). K.M.R., M.S., and P.S. (PNNL) and B.G. (LBNL) acknowledge the support from the U.S. Department of Energy (DOE) Office of Science, Office of Basic Energy Sciences, Chemical Sciences, Geosciences and Biosciences Division through its Geosciences programs at the Pacific Northwest National Laboratory (PNNL) and Lawrence Berkeley Laboratory (LBNL). The PNNL is a multiprogram national laboratory operated for DOE by Battelle Memorial Institute under Contract DE-AC05-76RL0-1830.

Notes and references

1. Mayousse C, Celle C, Fraczkiewicz A, Simonato JP. Stability of silver nanowire based electrodes under environmental and electrical stresses. Nanoscale. 2015;7(5):2107-15.

2. Singh I, Sabita P, Altekar VA. Silver tarnishing and its prevention — A review. Anti-Corrosion Methods and Materials. 1 janv 1983;30(7):4-8.

3. Simonnin P, Sassi M, Gilbert B, Charlet L, Rosso KM. Phase Transition and Liquid-like Superionic Conduction in Ag2S. J Phys Chem C. 7 mai 2020;124(18):10150-8.

4. Lu Q, Gao F, Komarneni S. Biomolecule-Assisted Synthesis of Highly Ordered Snowflakelike Structures of Bismuth Sulfide Nanorods. J Am Chem Soc. 1 janv 2004;126(1):54-5.

5. Nasrallah TB, Dlala H, Amlouk M, Belgacem S, Bernède JC. Some physical investigations on Ag2S thin films prepared by sequential thermal evaporation. Synthetic Metals. 15 août 2005;151(3):225-30.

6. Fu T. Silver sulfide-based sensor for the selective determination of ammonia at room temperature. Electrochimica Acta. 1 mars 2014;121:168-74.

7. Karashanova D. Crystalline structure and phase composition of epitaxially grown Ag2S thin films. Solid State Ionics. juill 2004;171(3-4):269-75.

8. El-Nahass MM, Farag AAM, Ibrahim EM, Abd-El-Rahman S. Structural, optical and electrical properties of thermally evaporated Ag2S thin films. Vacuum. 16 janv 2004;72(4):453-60.

9. Krylova V, Milbrat A, Embrechts A, Baltrusaitis J. Ag2S deposited on oxidized polypropylene as composite material for solar light absorption. Applied Surface Science. 15 mai 2014;301:134-41.

10. Parak WJ, Gerion D, Zanchet D, Woerz AS, Pellegrino T, Micheel C, et al. Conjugation of DNA to Silanized Colloidal Semiconductor

Nanocrystalline Quantum Dots. Chem Mater. 1 mai 2002;14(5):2113-9.

11. Peterson JJ, Krauss TD. Fluorescence Spectroscopy of Single Lead Sulfide Quantum Dots. Nano Lett. 1 mars 2006;6(3):510-4.

12. Chatterjee N. An internally consistent thermodynamic database on minerals: application to the Earth's crust and upper mantle. [UMI Dissertation Services]. [City Univ. New York]; 1989.

13. Jiang P, Zhu CN, Zhang ZL, Tian ZQ, Pang DW. Water-soluble Ag2S quantum dots for near-infrared fluorescence imaging in vivo. Biomaterials. 1 juill 2012;33(20):5130-5.

14. Rempel SV, Podkorytova AA, Rempel AA. Concentration quenching of fluorescence of colloid quantum dots of cadmium sulfide. Phys Solid State. 1 mars 2014;56(3):568-71.

15. Li C, Zhang Y, Wang M, Zhang Y, Chen G, Li L, et al. In vivo real-time visualization of tissue blood flow and angiogenesis using Ag2S quantum dots in the NIR-II window. Biomaterials. 1 janv 2014;35(1):393-400.

16. Etchable plasmonic nanoparticle probes to image and quantify cellular internalization | Nature Materials [Internet]. [cité 16 oct 2020]. Disponible sur: https://www.nature.com/articles/nmat3982

17. Goodman AM, Cao Y, Urban C, Neumann O, Ayala-Orozco C, Knight MW, et al. The Surprising in Vivo Instability of Near-IR-Absorbing Hollow Au–Ag Nanoshells. ACS Nano. 22 avr 2014;8(4):3222-31.

18. Le Ouay B, Stellacci F. Antibacterial activity of silver nanoparticles: A surface science insight. Nano Today. 1 juin 2015;10(3):339-54.

19. Wei L, Lu J, Xu H, Patel A, Chen ZS, Chen G. Silver nanoparticles: synthesis, properties, and therapeutic applications. Drug Discovery Today. 1 mai 2015;20(5):595-601.

20. Dos Santos CA, Seckler MM, Ingle AP, Gupta I, Galdiero S, Galdiero M, et al. Silver Nanoparticles: Therapeutical Uses, Toxicity, and Safety Issues. Journal of Pharmaceutical Sciences. 1 juill 2014;103(7):1931-44.

21. Zhang C, Hu Z, Deng B. Silver nanoparticles in aquatic environments: Physiochemical behavior and antimicrobial mechanisms. Water Research. 1 janv 2016;88:403-27.

22. Zazo H, Colino CI, Lanao JM. Current applications of nanoparticles in infectious diseases. Journal of Controlled Release. 28 févr 2016;224:86-102.

23. Ma R, Levard C, Judy JD, Unrine JM, Durenkamp M, Martin B, et al. Fate of Zinc Oxide and Silver Nanoparticles in a Pilot Wastewater Treatment Plant and in Processed Biosolids. Environ Sci Technol. 7 janv 2014;48(1):104-12.

24. Lehmann SG, Toybou D, Real AEP del, Arndt D, Tagmount A, Viau M, et al. Crumpling of silver nanowires by endolysosomes strongly reduces toxicity. PNAS. 23 juill 2019;116(30):14893-8.

25. Levard C, Hotze EM, Colman BP, Dale AL, Truong L, Yang XY, et al. Sulfidation of Silver Nanoparticles: Natural Antidote to Their Toxicity. Environ Sci Technol. 3 déc 2013;47(23):13440-8.

26. Misra SK, Dybowska A, Berhanu D, Luoma SN, Valsami-Jones E. The complexity of nanoparticle dissolution and its importance in nanotoxicological studies. Science of The Total Environment. 1 nov 2012;438:225-32.

27. Bennett JM, Stanford JL, Ashley EJ. Optical Constants of Silver Sulfide Tarnish Films*. J Opt Soc Am, JOSA. 1 févr 1970;60(2):224-32.

28. Elsaeedy HI. A low temperature synthesis of Ag2S nanostructures and their structural, morphological, optical, dielectric and electrical studies: An effect of SDS surfactant concentration. Materials Science in Semiconductor Processing. 1 avr 2019;93:360-5.

29. Suárez JA, Plata JJ, Márquez AM, Sanz JF. Structural, electronic and optical properties of

copper, silver and gold sulfide: a DFT study. Theor Chem Acc. 27 févr 2016;135(3):70.

30. Zhao Z, Wei H, Mao WL. Pressure tuning the lattice and optical response of silver sulfide. Appl Phys Lett. 27 juin 2016;108(26):261902.

31. Abufager PN, Lustemberg PG, Crespos C, Busnengo HF. DFT Study of Dissociative Adsorption of Hydrogen Sulfide on Cu(111) and Au(111). Langmuir. 16 déc 2008;24(24):14022-6.

32. Graedel TE, Franey JP, Gualtieri GJ, Kammlott GW, Malm DL. On the mechanism of silver and copper sulfidation by atmospheric H2S and OCS. Corrosion Science. 1 janv 1985;25(12):1163-80.

33. Liu J, Pennell KG, Hurt RH. Kinetics and Mechanisms of Nanosilver Oxysulfidation. Environ Sci Technol. 1 sept 2011;45(17):7345-53.

34. Thalmann B, Voegelin A, Morgenroth E, Kaegi R. Effect of humic acid on the kinetics of silver nanoparticle sulfidation. Environmental Science: Nano. 2016;3(1):203-12.

35. Elechiguerra JL, Larios-Lopez L, Liu C, Garcia-Gutierrez D, Camacho-Bragado A, Yacaman MJ. Corrosion at the Nanoscale: The Case of Silver Nanowires and Nanoparticles. Chem Mater. 1 nov 2005;17(24):6042-52.

36. Carlier D, Cheng JH, Pan CJ, Menetrier M, Delmas C, Hwang BJ. DFT plus U Calculations and XAS Study: Further Confirmation of the Presence of CoO_5 Square-Based Pyramids with IS-$Co^{3+\$}$ in Li-Overstoichiometric $LiCoO_2$. J Phys Chem C. 2013;117:26493-500.

37. Iacomino A, Cantele G, Trani F, Ninno D. DFT Study on Anatase TiO2 Nanowires: Structure and Electronic Properties As Functions of Size, Surface Termination, and Morphology. J Phys Chem C. 29 juill 2010;114(29):12389-400.

38. Sun S, Zhang D, Li C, Wang Y. DFT study on the adsorption and dissociation of H2S on CuO(111) surface. RSC Adv. 24 févr 2015;5(28):21806-11.

39. Russell SM, Kim Y, Liu DJ, Evans JW, Thiel PA. Communication: Structure, formation, and equilibration of ensembles of Ag-S complexes on an Ag surface. J Chem Phys. 15 févr 2013;138(7):071101.

40. Russell SM, Shen M, Liu DJ, Thiel PA. Adsorption of sulfur on Ag(100). Surface Science. 1 mars 2011;605(5):520-7.

41. Alfonso DR, Cugini AV, Sorescu DC. Adsorption and decomposition of H2S on Pd(111) surface: a first-principles study. Catalysis Today. 30 janv 2005;99(3):315-22.

42. Chen S, Sun S, Lian B, Ma Y, Yan Y, Hu S. The adsorption and dissociation of H2S on Cu(100) surface: A DTF study. Surface Science. 1 févr 2014;620:51-8.

43. Jiang DE, Carter EA. First principles study of H2S adsorption and dissociation on Fe(110). Surface Science. 20 mai 2005;583(1):60-8.

44. Jiang Z, Li M, Qin P, Fang T. Insight into the adsorption and decomposition mechanism of H2S on clean and S-covered Au (100) surface: A theoretical study. Applied Surface Science. 30 août 2014;311:40-6.

45. Hafner J, Kresse G. The Vienna AB-Initio Simulation Program VASP: An Efficient and Versatile Tool for Studying the Structural, Dynamic, and Electronic Properties of Materials. In: Gonis A, Meike A, Turchi PEA, éditeurs. Properties of Complex Inorganic Solids [Internet]. Boston, MA: Springer US; 1997. p. 69-82. Disponible sur: https://doi.org/10.1007/978-1-4615-5943-6_10

46. Paier J, Hirschl R, Marsman M, Kresse G. The Perdew–Burke–Ernzerhof exchange-correlation functional applied to the G2-1 test set using a plane-wave basis set. J Chem Phys. 15 juin 2005;122(23):234102.

47. Perdew JP, Burke K, Ernzerhof M. Generalized gradient approximation made simple. Phys Rev Lett. 1996;77:3865-8.

48. Blöchl PE. Projector augmented-wave method. Phys Rev B. 15 déc 1994;50(24):17953-79.

49. Tang W, Sanville E, Henkelman G. A grid-based Bader analysis algorithm without lattice bias. J Phys: Condens Matter. janv 2009;21(8):084204.

50. Sanville E, Kenny SD, Smith R, Henkelman G. Improved grid-based algorithm for Bader charge allocation. Journal of Computational Chemistry. 2007;28(5):899-908.

51. Henkelman G, Arnaldsson A, Jónsson H. A fast and robust algorithm for Bader decomposition of charge density. Computational Materials Science. 1 juin 2006;36(3):354-60.

52. Yu M, Trinkle DR. Accurate and efficient algorithm for Bader charge integration. J Chem Phys. 10 févr 2011;134(6):064111.

53. Sassi M, Oison V, Debierre JM. First principle study of a bimolecular thin film on Ag(111) surface. Surface Science. 1 sept 2008;602(17):2856-62.

54. Zhang Z, Liu T, Fu B, Yang X, Zhang DH. First-principles quantum dynamical theory for the dissociative chemisorption of H2O on rigid Cu(111). Nat Commun. 10 juin 2016;7(1):11953.

55. Hundt PM, Jiang B, van Reijzen ME, Guo H, Beck RD. Vibrationally Promoted Dissociation of Water on Ni(111). Science. 2 mai 2014;344(6183):504-7.

56. Gross A, Wilke S, Scheffler M. Six-Dimensional Quantum Dynamics of Adsorption and Desorption of ${\mathrm{H}}_{2}$ at Pd(100): Steering and Steric Effects. Phys Rev Lett. 2 oct 1995;75(14):2718-21.

57. Dai J, Light JC. Six dimensional quantum dynamics study for dissociative adsorption of H2 on Cu(111) surface. J Chem Phys. août 1997;107(5):1676-9.

58. Sementa L, Wijzenbroek M, van Kolck BJ, Somers MF, Al-Halabi A, Busnengo HF, et al. Reactive scattering of H2 from Cu(100): Comparison of dynamics calculations based on the specific reaction parameter approach to density functional theory with experiment. J Chem Phys. 28 janv 2013;138(4):044708.

59. Sheppard D, Henkelman G. Paths to which the nudged elastic band converges. Journal of Computational Chemistry. 2011;32(8):1769-71.

60. Sheppard D, Terrell R, Henkelman G. Optimization methods for finding minimum energy paths. J Chem Phys. 2 avr 2008;128(13):134106.

61. Henkelman G, Jónsson H. Improved tangent estimate in the nudged elastic band method for finding minimum energy paths and saddle points. J Chem Phys. 29 nov 2000;113(22):9978-85.

62. Henkelman G, Uberuaga BP, Jónsson H. A climbing image nudged elastic band method for finding saddle points and minimum energy paths. J Chem Phys. 29 nov 2000;113(22):9901-4.

63. Henkelman G, Jóhannesson G, Jónsson H. Methods for Finding Saddle Points and Minimum Energy Paths. In: Schwartz SD, éditeur. Theoretical Methods in Condensed Phase Chemistry [Internet]. Dordrecht: Springer Netherlands; 2002 [cité 15 oct 2020]. p. 269-302. (Progress in Theoretical Chemistry and Physics). Disponible sur: https://doi.org/10.1007/0-306-46949-9_10

1